Surface-tension-anisotropy measurements of succinonitrile and pivalic acid: Comparison with microscopic solvability theory

M. Muschol, D. Liu, and H. Z. Cummins
Department of Physics, City College of the City University of New York, New York, New York 10031
(Received 24 February 1992)

New determinations of the surface-tension-anisotropy parameter ε_4 of succinonitrile (SCN), pivalic acid (PVA), and a PVA–1%-ethanol mixture are reported. Effects of temperature gradients and crystal orientation are analyzed in detail. The experiments utilized numerical interpolation techniques previously employed by Dougherty and Gollub to enhance the digital image resolution. The values found for ε_4 in SCN, PVA, and PVA–1%-ethanol are 0.0055± 0.0015, 0.025±0.002, and 0.026±0.002, respectively. From these values, the selection parameter σ^*_{theor} predicted by microscopic solvability theory for the three-dimensional axisymmetric case was computed and compared to the σ^*_{expt} values determined directly from previous dendritic-growth experiments. We find that $\sigma^*_{\text{theor}}/\sigma^*_{\text{expt}}$ is 0.56±0.20 for SCN, and 2.14±0.50 for PVA. Possible sources for these discrepancies are discussed.
PACS number(s): 68.70.+w, 68.10.Cr, 61.50.Cj

I. INTRODUCTION

It has long been known that dendritic solidification of a crystal into its undercooled melt results in dendrites with tip radius ρ and growth velocity v uniquely determined by the undercooling. Until recently, however, the mechanism responsible for this pattern-selection process was not understood.

In 1947, Ivantsov [1] showed that if surface tension is neglected, the thermal-diffusion and energy-conservation (Stefan) equations governing dendritic growth are solved by a continuous family of parabolic needle crystals, with only the product ρv fixed by the undercooling. Introduction of surface tension as a perturbation to the Ivantsov solution led to the prediction of a maximum in the $v(\rho)$ curve, suggesting that this maximum velocity may correspond to the operating point selected by the system [2]. But this *maximum-velocity hypothesis* was disproved in 1976 by the precise succinonitrile experiments of Glicksman, Schaefers, and Ayers [3].

Subsequently, Langer and Müller-Krumbhaar analyzed the stability of parabolic dendrites, treating surface tension as a linearized perturbation, and found that the Ivantsov continuum divides into stable (fast) and unstable (slow) regions. They suggested the *marginal-stability hypothesis* that the operating point selected by the physical dendrite corresponds to the marginal-stability point dividing the stable and unstable regions of the Ivantsov continuum. This hypothesis led to a selection rule for the quantity

$$\sigma = \frac{2d_0 D}{\rho^2 v}, \tag{1.1}$$

where D is the thermal-diffusion constant and d_0 is the capillary length defined as $d_0 = \gamma_0 T_m C_p / L^2$ (γ_0 is the surface tension, C_p the specific heat per unit volume, T_m the bulk melting temperature, and L the latent heat of fusion). For cubic crystals, they found that the value of the stability parameter σ^* selected by this mechanism was $\sigma^* \sim 0.026$, and they showed that $\sigma^* = 0.025$ produced a good fit to the experimentally determined selected velocities for both succinonitrile and ice, spanning a range in v of over five decades [2].

A new development in the theory of dendritic pattern selection occurred in a series of papers beginning in 1983, first with simplified local models, and later with the full nonlinear nonlocal equations of dendritic growth, in which surface tension was included from the outset. These theoretical investigations, utilizing both numerical and analytical methods, led to several surprising new insights: (i) surface tension constitutes a singular perturbation which destroys the continuum of Ivantsov solutions, replacing it with a discrete set; (ii) of this discrete set of allowed solutions, all but the fastest one are linearly unstable; (iii) the growth velocity of the single allowed stable solution depends critically on the anisotropy ε of the surface tension. For small values of ε, v is proportional at fixed undercooling to $\varepsilon^{7/4}$. This theoretical approach is frequently designated as *microscopic-solvability theory* (MST) because the presence of the microscopic capillary length d_0 imposes a solvability condition on a family of macroscopic steady-state solutions (for reviews, see Refs. [4–7]). MST showed that the quantity σ introduced in Eq. (1.1) was still the central selection parameter but the selected value depended on the crystalline surface-tension anisotropy ε of the material.

The selected values σ^* of Eq. (1.1) as a function of anisotropy ε have been computed both by numerical solution of the appropriate integro-differential equation and by several analytical techniques. Barbieri and Langer [8] computed σ^* analytically for both two-dimensional and three-dimensional axisymmetric dendrites, for both symmetric and nonsymmetric diffusion. In Fig. 1 we show

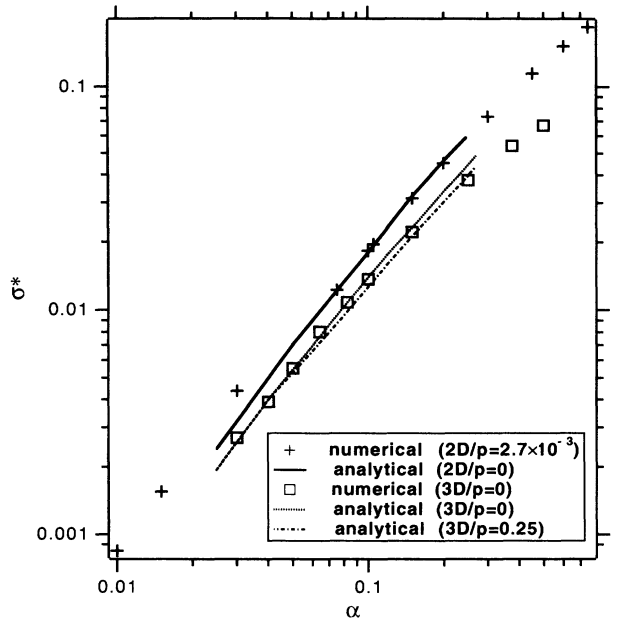

FIG. 1. Selected values of the stability parameter σ^* vs surface-tension anisotropy α predicted by microscopic solvability theory. (For fourfold anisotropy, $\alpha = 15\varepsilon_4$; for sixfold anisotropy, $\alpha = 35\varepsilon_6$.) The solid lines are the analytic results of Barbieri and Langer [8] for the symmetric model in two dimensions with $p = 0$ (—), in three dimensions with $p = 0$ (- - -), and in three dimensions with $p = 0.25$ (- · - · - ·). The symbols (+) are the results of a numerical calculation based on the method of Kessler and Levine [9] for the two-dimensional symmetric model with $p = 0.0027$, and the symbols (□) are the results of a numerical calculation by Ben Amar for a 3D axisymmetric model with $p = 0$.

their analytically computed results for symmetric growth in the small undercooling limit in two and three dimensions, a two-dimensional (2D) numerical result obtained with the method of Kessler and Levine [9] (the computer program used was generously provided by H. Levine), and the results of a 3D axisymmetric numerical computation by Ben Amar [10].

It has frequently been asserted that MST has definitively resolved the dendritic pattern-selection problem. However, there are several reasons for caution. First, the underlying set of continuum equations, though obviously difficult to solve, is nevertheless only approximate. They ignore the effects of microscopic crystal structure and growth kinetics, and they do not include the effects of noise and sidebranching, which may play a particularly significant role at very small anisotropies. Second, and of central interest in this report, attempts to establish the validity of MST by direct experimental tests have led to disappointingly uneven results. The source of this difficulty could well lie in the extreme dependence of σ^*_{theor} on surface-tension anisotropy in MST illustrated in Fig. 1, combined with the difficulty of obtaining experimental values of the anisotropy sufficiently precise to permit definitive tests of the theory.

To date, experimentally determined surface-tension anisotropies have been reported for only five materials: succinonitrile (SCN), pivalic acid (PVA), hectaoctyloxytriphenylene (HET), NH_4Br, and ice. Of these, only the anisotropy of PVA has been measured twice, and the two reported values differ by almost an order of magnitude. In the upper part of Table I we list the existing published anisotropy values for these materials with the predicted σ^*_{theor} values found from the data of Fig. 1, and compare these with the σ^*_{expt} values determined from direct observation of growing dendrites summarized in Table II. Clearly, no meaningful conclusion on the validity of MST can be reached from these results.

In this report, we present experimental determinations of the surface-tension anisotropy of SCN, PVA, and PVA–1% ethanol. Previous studies have been based on the observed shape of either a small crystal surrounded by the melt [11–13] or of a melt inclusion within a crystal [14, 15]. We used the small-crystal method, but improved the accuracy of our measurements by exploiting

TABLE I. σ^*_{theor} computed from experimentally determined surface anisotropy $\gamma(\theta) = \gamma_0[1 + \varepsilon_m \cos(m\theta)]$ and compared with σ^*_{expt}.

Material	Ref.	m	ε_m(%)	$\alpha = (m^2-1)\varepsilon_m$	σ^*_{theor}	σ^*_{expt}	Ref.
			(a) Previous measurements				
SCN	[14]	4	0.5	0.075	0.009	0.0195	[29]
PVA	[15]	4	5	0.75	0.14	0.022	[15]
PVA + 1% ethanol	[12]	4	0.6 ±0.2	0.09±0.03	0.024±0.010	0.05±0.02	[12]
NH_4Br (soln.)	[11]	4	1.6±0.4	0.24±0.06	0.072±0.018	0.081±0.020	[11]
HET (soln.)	[13]	6	0.3±0.1[a]	0.11±0.04	0.033±0.014	0.038	[13]
Ice	[24]	6	0.2±0.1	0.07±0.03	0.012±0.005[b]	≈0.075	[24]
			(b) This work				
SCN		4	0.55±0.15	0.083±0.023	0.011±0.004	0.0195	[29]
PVA		4	2.5±0.2	0.375±0.03	0.054±0.004	0.022	[15]
PVA+1% ethanol		4	2.6±0.2	0.390±0.03	0.107 ±0.007	0.05±0.02	[12]

[a] This value is 35 times smaller than that cited in Ref. [13] and corresponds to their Eq. (5) being revised to read $R(\theta) = R_0[1 - \varepsilon_6 \cos(6\theta)]$.

[b] We accounted for the asymmetry of the ice-water phases ($\mu \simeq 0.5$).

TABLE II. Experimentally determined σ^*_{expt} from dendritic growth experiments. $\sigma^*_{\text{expt}} = 2d_0D/v\rho^2$; p is the Péclet number; and m is the order of rotational symmetry.

Material	σ^*_{expt}	p	m	Ref.
SCN	0.0195	2×10^{-4}–3×10^{-2}	4	[29]
PVA	0.022	$9\times10^{-4}-1\times10^{-3}$	4	[15]
PVA + 1% ethanol	0.05 ± 0.02	$8\times10^{-3}-5\times10^{-2}$	4	[12]
NH_4Br (soln.)	0.081 ± 0.020	$5\times10^{-4}-2\times10^{-3}$	4	[11]
NH_4Br (soln.)	0.072 ± 0.037	$1\times10^{-3}-5\times10^{-3}$	4	[30]
HET	0.038	3×10^{-3}	6	[13]
Ice	0.025		6	[2,31]
Ice	0.075[a]	$5\times10^{-5}-2\times10^{-3}$	6	[24]
Helium	0.0013	$2\times10^{-3}-2\times10^{-2}$	4	[32]
Krypton	0.017 ± 0.009	$2\times10^{-5}-1\times10^{-3}$	4	[33]
Xenon	0.022 ± 0.012	$1\times10^{-5}-8\times10^{-4}$	4	[33]

[a] From Fig. 13 in Ref. [24].

the stabilizing effect of a temperature gradient. Incorporating digital interpolation techniques similar to those of Ref. [11] in our videomicroscopy image-analysis procedures helped us to push the effective resolution down to approximately 0.2 pixels. Since we are studying two-dimensional projections of small three-dimensional crystals, we have developed a method to determine the orientation of the crystal axes before measuring the shape. As we shall show, the apparent anisotropy of such a crystal depends strongly on its orientation, so that experiments with uncontrolled orientations would produce wide variation in the measured anisotropy.

In Sec. II, we review the equations governing the shape of a crystal in equilibrium with its undercooled melt, first for uniform undercooling, and then with an added temperature gradient. We also consider the relation of this two-dimensional analysis to observations of three-dimensional crystals. In Sec. III, we describe our experimental methods and data-analysis procedures and present a summary of our results. In the concluding section, Sec. IV, we discuss our results in comparison with previously published anisotropy values and discuss the implications for MST.

II. THEORY OF SHAPE ANISOTROPY

A. Uniform undercooling

The shape of a crystal in equilibrium with its melt is controlled by the Gibbs-Thompson equation which determines the lowering of the equilibrium interface temperature T_i relative to the bulk melting temperature T_m due to the curvature κ of the interface. In two dimensions,

$$T_i = T_m[1-(\gamma+\gamma_{\theta\theta})\kappa/L], \tag{2.1}$$

where $\gamma(\theta)$ is the orientation-dependent surface tension, θ is the angle of the interface normal to the crystal axis, $\gamma_{\theta\theta}$ is the second derivative of $\gamma(\theta)$ with respect to θ, and κ is the curvature of the solid-liquid interface [16]. If γ is isotropic and the melt is uniformly undercooled, Eq. (2.1) shows that κ must be constant so that the equilibrium crystal will be circular with radius $R = 1/\kappa$ given by $R^* = \gamma/L\Delta$, or $R^* = (d_0/\Delta)(L/T_mC_p)$ where we have defined the dimensionless undercooling $\Delta = (T_m-T)/T_m$ [17]. Note that this R^* is just the critical radius of nucleation, the minimum size that a crystal must reach to overcome the nucleation barrier. Crystals with $R < R^*$ will melt, while those with $R > R^*$ will grow, so that $R = R^*$ represents a state of unstable equilibrium.

For a weakly anisotropic crystal with m-fold rotational symmetry, the surface tension $\gamma(\theta)$ is usually approximated by a constant plus the lowest-order θ-dependent term allowed by symmetry:

$$\gamma(\theta) = \gamma_0[1+\varepsilon_m\cos(m\theta)]. \tag{2.2}$$

Combining Eqs. (2.1) and (2.2), an approximate solution for the interface $R(\phi)$ can be found (where R, ϕ are the polar coordinates of the interface):

$$R(\phi) = R^*[1+\varepsilon_m\cos(m\phi)], \tag{2.3}$$

where, again, $R^* = \gamma/L\Delta$ is the critical radius of nucleation. Note that in this approximation, the relative amplitude of the $\cos(m\phi)$ shape anisotropy is identical to that of the γ anisotropy. Since most materials used in dendritic solidification studies are cubic, the most important case is $m = 4$.

Equations (2.1) and (2.2) can also be solved exactly by first converting Eq. (2.1) to a pair of first-order parametric differential equations [18]. Their solutions are

$$x = [\gamma\cos(\theta) - \gamma_\theta\sin(\theta)]/\Delta L, \tag{2.4}$$

$$y = [\gamma\sin(\theta) + \gamma_\theta\cos(\theta)]/\Delta L. \tag{2.5}$$

Substituting Eq. (2.2) for $m = 4$ into Eqs. (2.4) and (2.5) with different values of ε_4 then produces a series of interface shapes as shown in Ref. [18]. For $\varepsilon_4 = 0$, the interface is round. As ε_4 increases, increasingly prominent bulges appear along the four axes, effectively reducing

the fraction of the interface for which $\varepsilon_4 \cos(4\theta)$ is largest. Cusps appear on the surface when $\gamma+\gamma_{\theta\theta}=0$ [$\varepsilon_4 = 1/15$ or more generally $\varepsilon_m = (m^2-1)^{-1}$]; for $\varepsilon_m > 1/15$, some orientations are missing. Thus, 1/15 represents the upper limit on ε_4 for this approach. Alternatively, by using $\alpha = (m^2-1)\varepsilon_m$ as the anisotropy parameter, this upper limit corresponds to $\alpha = 1$ independent of m (see Fig. 1).

In order to compare the exact and approximate solutions to Eqs. (2.1) and (2.2), we generated polar plots $R(\phi)$ of Eqs. (2.4) and (2.5) for different values of ε_4. These were then Fourier analyzed as

$$R(\phi) = R_0[1 + \sum_k s_k \cos(k\phi)]. \tag{2.6}$$

The resulting values of the fourfold shape anisotropy s_4 divided by the prediction $s_4 = \varepsilon_4$ of the approximate solution [Eq. (2.3)] are shown in Fig. 2 as s_4/ε_4 vs ε_4. Up to the maximum value of $\varepsilon_4 = 1/15$ at which cusps would appear, the maximum disagreement is $< 10\%$, while for ε_4 values less than 0.03 with which we will be concerned, the two results agree to better than 2%. The only other Fourier component with significant amplitude was $\cos(8\phi)$ whose amplitude reaches almost 20% of the (4ϕ) component at $\varepsilon_4 = 1/15$. (s_8/ε_4 is also shown in Fig. 2.)

B. Temperature gradient

Next, consider a crystal located in a radially symmetric linear temperature gradient G so that, in polar coordinates (r, ϕ),

$$T(r) = T_0 + Gr. \tag{2.7}$$

Since at equilibrium the interface temperature T_i of Eq. (2.1) must equal the local $T(r)$ of Eq. (2.7), we have

$$T_0 + Gr = T_m[1 - (\gamma + \gamma_{\theta\theta})\kappa/L]. \tag{2.8}$$

Guided by the approximate solution [Eq. (2.3)] for the constant temperature case, we first look for an approximate solution to Eq. (2.8) of the form

$$R(\phi) = R_0[1 + s_4 \cos(4\phi)]. \tag{2.9}$$

Assuming that the shape anisotropy factor s_4 is small and that the difference between the polar angle ϕ and the normal angle θ can be ignored, we obtain, for the curvature of $R(\theta)$ to first order in s_4,

$$\kappa(\theta) \sim (1/R_0)[1 + 15 s_4 \cos(4\theta)]. \tag{2.10}$$

Combining Eqs. (2.2), (2.8), and (2.10) for the case $m = 4$, and collecting terms in ascending orders in s_4, we find

$$T_0 + GR_0 = T_m(1 - \gamma_0/LR_0), \tag{2.11}$$

$$-(G/T_m)s_4 R_0 = (15\gamma_0/LR_0)(s_4 - \varepsilon_4). \tag{2.12}$$

Equation (2.11) determines the average radius R_0. If G=0 it reduces to $R_0 = \gamma/L\Delta$, as found above in the isotropic uniform undercooling case. With the gradient included, however, Eq. (2.11) is a quadratic equation in R_0 which may have zero, one, or two solutions. In Fig. 3, we have plotted the two sides of Eq. (2.11) separately for the case where there are two solutions. The smaller solution R_u is unstable since a small increase in R will bring the crystal surface to a position where the local temper-

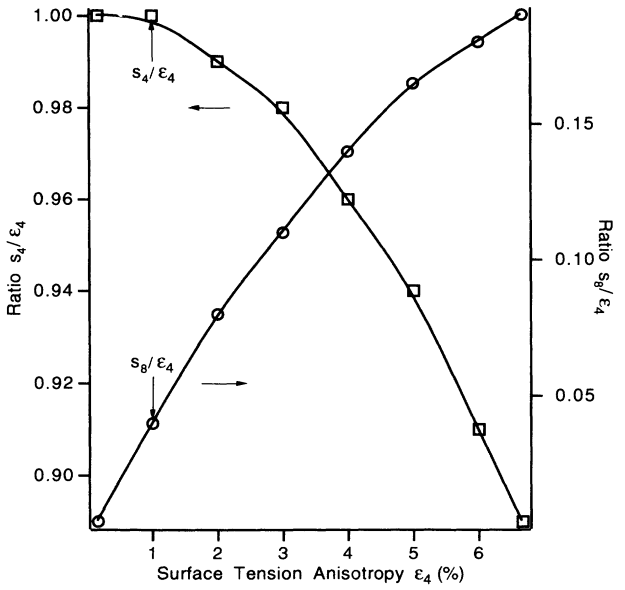

FIG. 2. Fourier amplitudes s_4 and s_8 of the analytical solutions of Eqs. (2.4) and (2.5) using the surface tension form of Eq. (2.2). Both s_4 and s_8 are normalized to ε_4 and plotted against ε_4. Note that for $\varepsilon_4 < 0.03$, s_4 and ε_4 agree to better than 2%. (The solid lines are guides to the eye.)

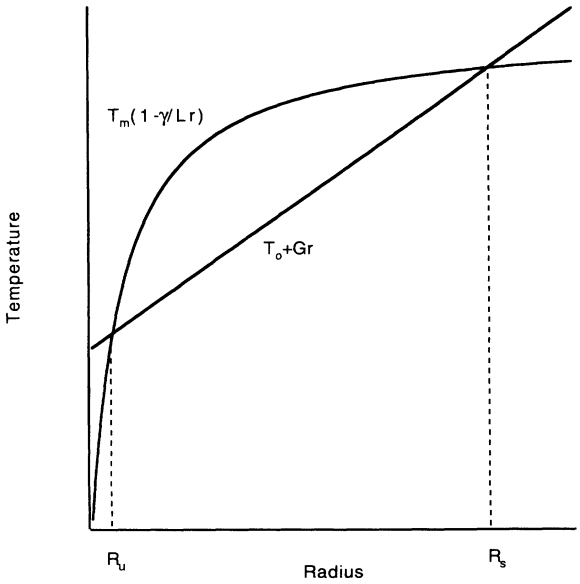

FIG. 3. Plots of the two sides of Eq. (2.11) indicating two solutions at $r = R_u$ and R_s. Note the different stabilities of the two solutions.

ature $T_0 + GR$ is below the surface melting temperature, and the crystal will grow. Similarly, a decrease in R will cause the crystal to melt. This solution, therefore, corresponds to the usual unstable solution in the uniform undercooling case. Conversely, the second solution at R_s is absolutely stable.

Equation (2.12) shows that the temperature gradient suppresses the shape anisotropy relative to the uniform undercooling case where $s_4 = \varepsilon_4$. This result is physically reasonable since the bulges will now extend into a warmer region of the melt and will therefore be reduced relative to the uniform undercooling case.

It is useful to rewrite Eq. (2.12) in the form

$$s_4/\varepsilon_4 = [1 + G/(15G_c)]^{-1}, \tag{2.13}$$

where $G_c = \gamma_0 T_m / L R_0^2$ has the dimensions of a temperature gradient. In Fig. 4(a) we plot s_4/ε_4 vs G as found from Eq. (2.13) for crystals with radii between 50 and 1000 μm, all with anisotropy of $\varepsilon_4 = 0.05$. The shape anisotropy is more strongly suppressed for the larger crystals, as expected, since their bulges extend farther into the higher-temperature region. If we scale the gradient G by G_c, Eq. (2.13) then predicts a universal plot for s_4/ε_4 as shown by the solid line in Fig. 4(b). This figure also shows that the shape anisotropy is not significantly affected by the gradient until G is well above G_c.

The physical significance of the critical gradient G_c can be found from the Gibbs-Thompson equation (2.1) for isotropic surface tension where the interface temperature T_i and equilibrium radius R_0 are related by $T_i = T_m[1 - \gamma/Lr]_{r=R_0}$. The derivative of T_i with respect to r, evaluated at $r = R_0$, is then

$$(dT_i/dr)_{R_0} = \gamma T_m / L R_0^2. \tag{2.14}$$

Equation (2.14) shows that G_c is just the slope of the melting point curve at the radius R_0. As can be seen from Fig. 3, $G < G_c$ implies an unstable solution, while $G > G_c$ implies a stable one. Note, however, that even for unstable solutions with $G < G_c$, the presence of a gradient will reduce the instability, increasing the time it takes for a crystal with $R = R_u$ to grow or shrink appreciably.

Finally, we solved Eq. (2.8) numerically in order to test the limits of validity of the approximate solution of Eqs. (2.11)–(2.13). Again, as in the uniform undercooling case, Eq. (2.8) was reduced to a pair of first-order parametric differential equations which were solved numerically by a relaxation method [19]. Details of the calculation will be presented elsewhere [20]. Interface profiles were calculated for a wide range of gradients, with anisotropies of ε_4= 0.01, 0.03, 0.04, and 0.05. The resulting values for the shape-anisotropy parameter s_4 are indicated by the symbols in Fig. 4(b) and are seen to be in excellent agreement with the approximate result of Eq. (2.13). In fact, for $G < G_c$, all the results are indistinguishable from the simple uniform undercooling result of Eq. (2.3).

C. Extension to three dimensions

So far we have discussed the equilibrium shape and stability properties of a two-dimensional crystal at uniform undercooling as well as in the presence of a linear, radially symmetric temperature gradient. Experimentally we observe two-dimensional projections of three-dimensional crystals. In three dimensions the Gibbs-Thompson relation [given for two dimensions in Eq. (2.1)] is [16]

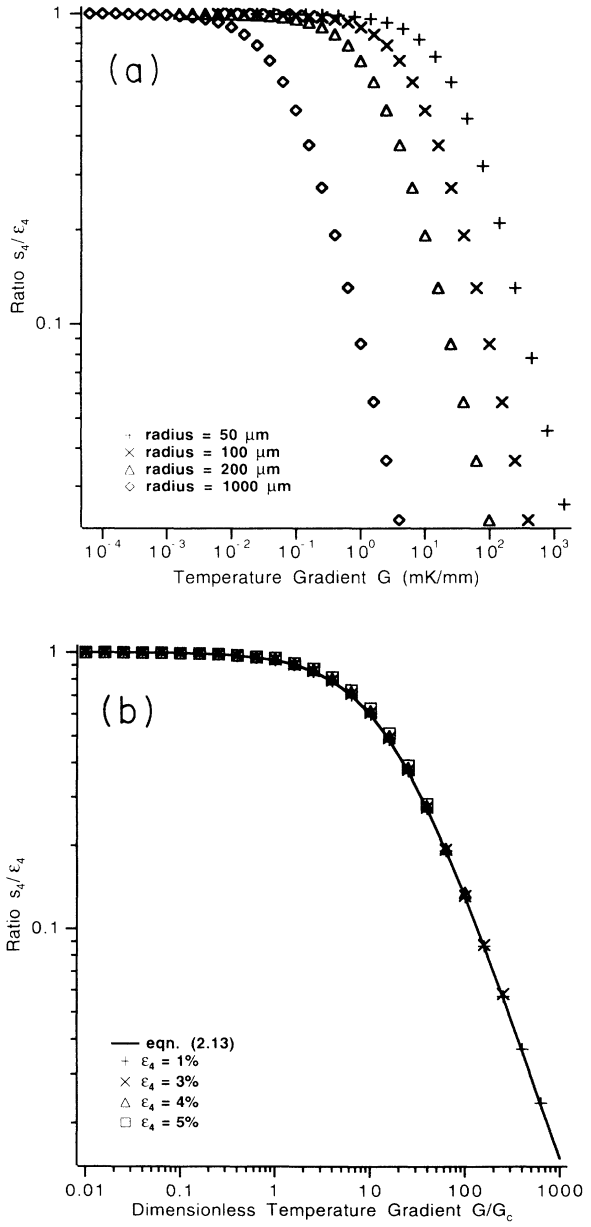

FIG. 4. (a) Influence of a temperature gradient G on the shape anisotropy for crystals of different size. The material parameters used to generate these plots where those of SCN and the anisotropy was choosen to be $\varepsilon_4 = 5\%$. (b) Data similar to (a) for four values of ε_4 plotted against the dimensionless gradient G/G_c. The solid line is the scaling prediction of Eq. (2.13).

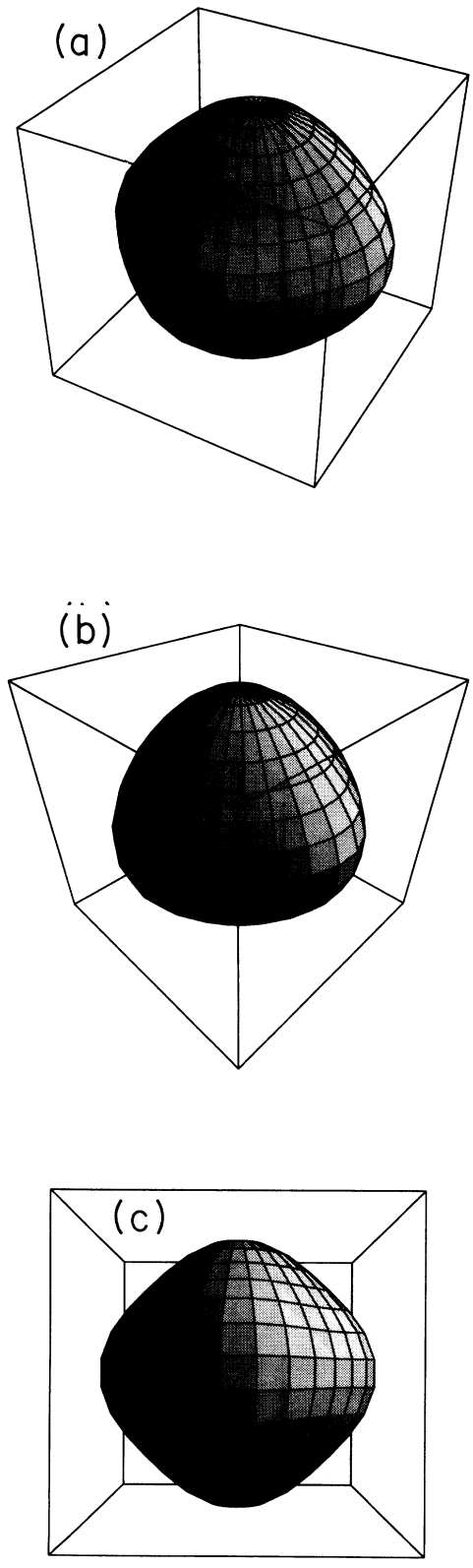

FIG. 5. Three views of the three-dimensional anisotropic surface tension function $\gamma(\theta,\phi)$ of Eq. (2.16) for $\varepsilon_4 = 0.05$. In (b), the normal is along a [111] axis, while in (c) it is along a [100] axis.

$$T_i = T_m\{1 - [(\gamma + \gamma_{\theta_1\theta_1})\kappa_1 + (\gamma + \gamma_{\theta_2\theta_2})\kappa_2]/L\}, \tag{2.15}$$

where θ_1 and θ_2 are the angles along the principal axes of the surface and R_1 and R_2 are the corresponding principal curvatures. The three-dimensional equivalent to the approximate fourfold-symmetric surface-tension expression of Eq. (2.2) is the cubic symmetric function [4]

$$\gamma(\theta,\phi) = \gamma_0[1 + \varepsilon_4(4\{\sin^4(4\phi)[\cos^4(4\theta) + \sin^4(4\phi)] + \cos^4(4\theta)\} - 3)], \tag{2.16}$$

where $\theta \in [0,\pi]$ and $\phi \in [0,2\pi]$ are the usual polar angles in spherical coordinates. Figure 5 shows three plots of this function from different angles. Note that we have slightly altered the form of $\gamma(\theta,\phi)$, as given in Ref. [4], so that Eq. (2.16) goes over into Eq. (2.2) in the x-y plane ($\theta = \pi/2$), the x-z plane ($\phi = 0$), or the y-z plane ($\phi = \pi/2$). The shape of the corresponding three-dimensional crystal at uniform undercooling was derived by Cahn and Hoffmann [21] and can be expressed in Cartesian coordinates by [18]

$$x = 2[\gamma\sin(\theta)\cos(\phi) + \gamma_\theta\cos(\theta)\cos(\phi) - \gamma_\phi\sin(\phi)/\sin(\theta)]/L\Delta, \tag{2.17}$$

$$y = 2[\gamma\sin(\theta)\sin(\phi) + \gamma_\theta\cos(\theta)\sin(\phi) - \gamma_\phi\cos(\phi)/\sin(\theta)]/L\Delta \tag{2.18}$$

$$z = 2[\gamma\cos(\theta) - \gamma_\theta\sin(\theta)]/L\Delta. \tag{2.19}$$

For small ε_4, the equilibrium shape of the three-dimensional crystal will again be equivalent to the γ plot of Eq. (2.16). A projection of $\gamma(\theta,\phi)$ along the [111] direction will show three- and sixfold components [see Fig. 5(b)] and give anomalously small values for ε_4. Only if the crystal is oriented with one axis vertical, as in Fig. 5(c), will the values we extract for ε_4 using a two-dimensional model [Eq. (2.6)] to analyze the projections of a three-dimensional crystal produce the correct value for the surface-tension anisotropy.

III. EXPERIMENTAL PROCEDURES AND RESULTS

Our essential procedure was to establish a single small, properly oriented crystal in equilibrium with its surrounding melt, record the shape of the crystal-melt interface by videomicroscopy with a charge-coupled-device (CCD) videocamera, and generate digital images of it with a computer-based video board. The digital images were further processed to obtain an accurate set of polar interface coordinates (r_i,ϕ_i). Fourier analysis of these data then allowed us to extract the value of the surface-tension anisotropy ε_4 for that crystal following Eq. (2.3).

A. Apparatus

1. Sample preparation

The experiments were performed with three different types of samples: pure SCN, pure PVA, and a binary sample of PVA and 1% ethanol by weight. The starting materials for our sample preparation, SCN (Fluka, 99%) and PVA (Aldrich Chemicals, 99%) were vacuum distilled four times at 110 °C and 60 °C, respectively. The purified materials were transferred to carefully cleaned glass capillaries with 4×0.2 mm inside cross section, approximately 30 cm long (Vitro Dynamics). After sealing one end of the capillary with a torch, we push the open end through a rubber seal on a glass stopper in one port of a multineck flask. The flask is then evacuated and the purified material distilled into it. The capillary is dipped into the molten material and, after disconnecting the vacuum pump, the flask is slowly backfilled with helium to force the molten material into the capillary. Finally, the capillary is pulled out of the liquid and the flask is put back under vacuum. The capillary is then sealed off under vacuum with a miniature torch, and is further divided into two or three samples of 5 cm length and a cross section of 4×0.2 mm for the experiments.

The sample preparation for the binary PVA-ethanol mixture was slightly different. After purifying the PVA, we distill it into a 25-ml buret with Teflon stopcocks on both ends, add a small amount of 200-proof ethanol from a previously sealed bottle to the buret, and mix both materials thoroughly with a miniature magnetic stirring bar. The buret is then placed on top of the multineck receiving flask and emptied into it.

We have found that the SCN samples, prepared as described above, have a melting point that is within 5 mK of the melting temperature of a SCN triple-point cell developed by Glicksman and purchased from the National Institute of Standards and Technology. Using the depression of the melting point for an ideal solution

$$T_m(0) - T_m(X) = (R_g T_m^2/L)X, \tag{3.1}$$

where R_g is the gas constant and X is the mol fraction of impurity, we estimate the purity to be better than 99.995%. We also estimated the purity of the SCN samples from their observed stability in a directional-solidification apparatus which gave an upper limit on the impurity concentration [22] of about 10^{-3}%, consistent with the melting-point result. For the PVA samples, we determined the melting point with a thermocouple to be $T_m = 35.9$ °C, which agrees within experimental accuracy with the melting temperature of $T_m = 35.935$ °C reported by Glicksman and Singh [15]. Finally the melting temperature of the binary PVA-ethanol mixture was $T_m = 30.3$ °C. These hermetically sealed glass capillaries showed no signs of aging. Further relevant material parameters are listed in Table III.

TABLE III. Material parameters for SCN and PVA employed in this work.

Parameter	SCN	Ref.	PVA	Ref.
γ (J/cm^2)	8.94×10^{-7}	[34]	2.84×10^{-7}	[36]
T_m (K)	331.23	[3]	309.09	[14]
L (J/cm^3)	46.7	[35]	20.7	[36]
L/C_p (K)	23.1	[3]	11.1	[14]

2. Thermostat and temperature control

Our thermostat is designed to fit onto the stage of our Nikon Diaphot microscope. It consists of an outer aluminum shell, controlled by a YSI-72 proportional temperature controller to within ±5 mK, and an inner copper shell, controlled by a Tronac PTC-41 temperature controller to within ±0.5 mK. The sample capillary is positioned inside of the inner shell, between two 1.6-mm-thick glass plates, surrounded by paraffin oil for heat transfer and optical index matching. Both thermostats have a flat cylindrical shape with a round opening of 20 mm diameter in the center, covered by glass windows. These windows produce a small heat loss at the center of the thermostat and lead to a radially symmetric variation of the temperature throughout the thermostat. We measured the radial temperature dependence by positioning a thermistor in different parts of the sample space of the inner shell. A typical temperature profile is shown in Fig. 6. The crystals can be trapped in the trough of this temperature profile. The estimated gradient at the boundary of a crystal of 100 μm radius is of the order of 10^{-4} mK/μm.

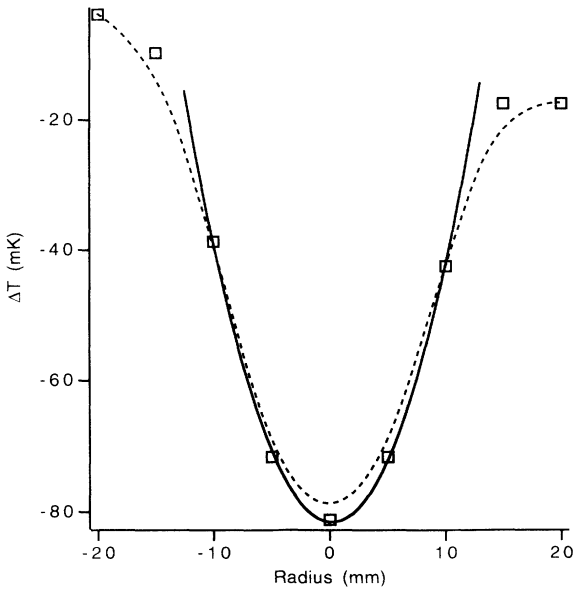

FIG. 6. Radial temperature profile of the sample space in the inner shell of the sample thermostat. The radius origin is the center of the observation window whose edges are at $r = \pm 10$ mm. The squares are the measured temperature deviations relative to the uniform temperature inside the copper shell of the thermostat. The solid line is a parabolic fit to the five center points and yields $T(r) = -81.5$ mK $+0.409$ (mK/mm^2)$(r - 0.189)^2$ where r is in mm.

3. *Microscope and video system*

The microscope we used is a Nikon Diaphot with inverted optics. It has a 35-mm-camera port and a video-camera port. We typically use it with a 10× long working distance objective and a 2.5× projection lens in the video port. The images are recorded with a Dage MTI-72 CCD camera. The video images are digitized with a 640×480 pixel Data Translation QuickCapture video board inside a Mac II computer. We also record the images on a Mitsubishi U31 commercial video-cassette recorder for later analysis.

We tested our camera and image system by capturing images of a circular reticle. Although we measured no geometric distortion of the field, the x scale of the image pixels was noticeably different from the y scale. With our 10× objective and 2.5× projector combination we determined scale factors of 0.59±0.01 μm/pixel in the x direction and of 0.62±0.01 μm/pixel in the y direction. After correcting for this difference we always obtained perfectly round images of our reticle independent of the orientation of the reticle or the camera.

B. Procedure

In a typical experimental run, the outer shell of the thermostat was first heated to a temperature 5 to 10 K below the melting temperature of the sample (in the case of PVA-ethanol the outer shell is not heated) and the inner shell was then heated until the whole sample was completely molten. We then cool the sample until it starts to solidify by spontaneous nucleation of crystallites, producing numerous small single-crystal grains which have no time to form multiple-grain structures.

When warming the sample back up close to its melting temperature, the grains close to the center of the observation window melt last, due to the temperature dip in the center of the thermostat (Fig. 6). We are usually able to capture a single-crystal grain in the center of the capillary. Then we quickly undercool it. For PVA, the orientation of the dendritic arms that shoot out from the initially round seed allows us to assess the orientation of the crystal (see Fig. 7). Next we shrink it back to a radius of about 80–100 μm, which is convenient for our observations. We were not able to accurately determine the orientation of our SCN seeds with this procedure since after rapid cooling they usually exhibited a dense-branching morphology rather than clearly developed dendritic arms.

Once the crystal is at an appropriate size for observation, it still tends to either grow or shrink slowly at fixed temperature. This is due to the fact that the critical gradient G_c needed to stabilize a 100-μm crystal is about one to two orders of magnitude larger than the largest gradients we can achieve in our sample thermostat (see Fig. 6). We allow the crystal to slowly grow (shrink) until its size becomes too large (small) for observation, at which point we raise (lower) the temperature of the inner thermostat to reverse the direction. Using this method we can observe a crystal for several hours. We generally find that after at most one hour the results of our shape measurements (for radii < 150 μm) remain constant, independent of the size of the crystal, the growth speed, or the direction of growth. Images of SCN, PVA, and PVA-ethanol crystal grains obtained this way are shown in Fig. 8.

C. Digital image analysis

The captured images consist of a rectangular array of 640×480 pixels, each pixel having an intensity resolution of 256 gray scales. The outline of the crystal interface appears as a thin dark line, 3–5 pixels wide, against a uniform lighter background. A radial intensity scan across

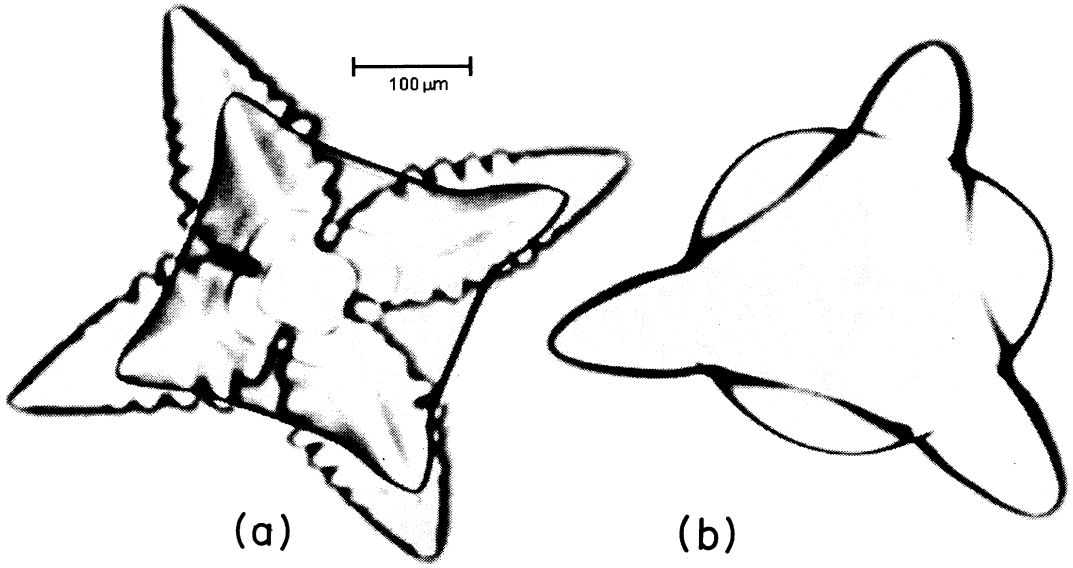

FIG. 7. Images of PVA crystals following a sudden temperature decrease. The fourfold symmetry of (a) indicates that this crystal is oriented with a [100] axis normal to the image, while the threefold symmetry of (b) indicates that a [111] axis is normal to the image.

such an interface is shown in Fig. 9, and we see that the profile is approximately parabolic.

We want to extract a set of polar coordinates (r_i, ϕ_i) of the crystal-melt interface from these images. To do so we first need to find the center of the crystal and then determine the radial distance r_i of the interface for a given orientation ϕ_i. As a first step we threshold the images: all pixels with intensity values close to the white background are disregarded and the preliminary center of the crystal is chosen to be the "center of mass" of all pixels above the threshold. From this preliminary center the interface is divided into angular slices of $2° - 3°$ width. The intensity profile $I(r)$ of all pixels within a given angular slice is fitted to a parabola (see Fig. 9). The distance of the maximum of this intensity parabola from the center is taken as the radial coordinate of the interface. We use the "center of mass" of these first-pass interface coordinates $[r_i(1), \phi_i(1)]$ to determine a more accurate location for the center. After running through this loop three times the corrections to the interface coordinates become

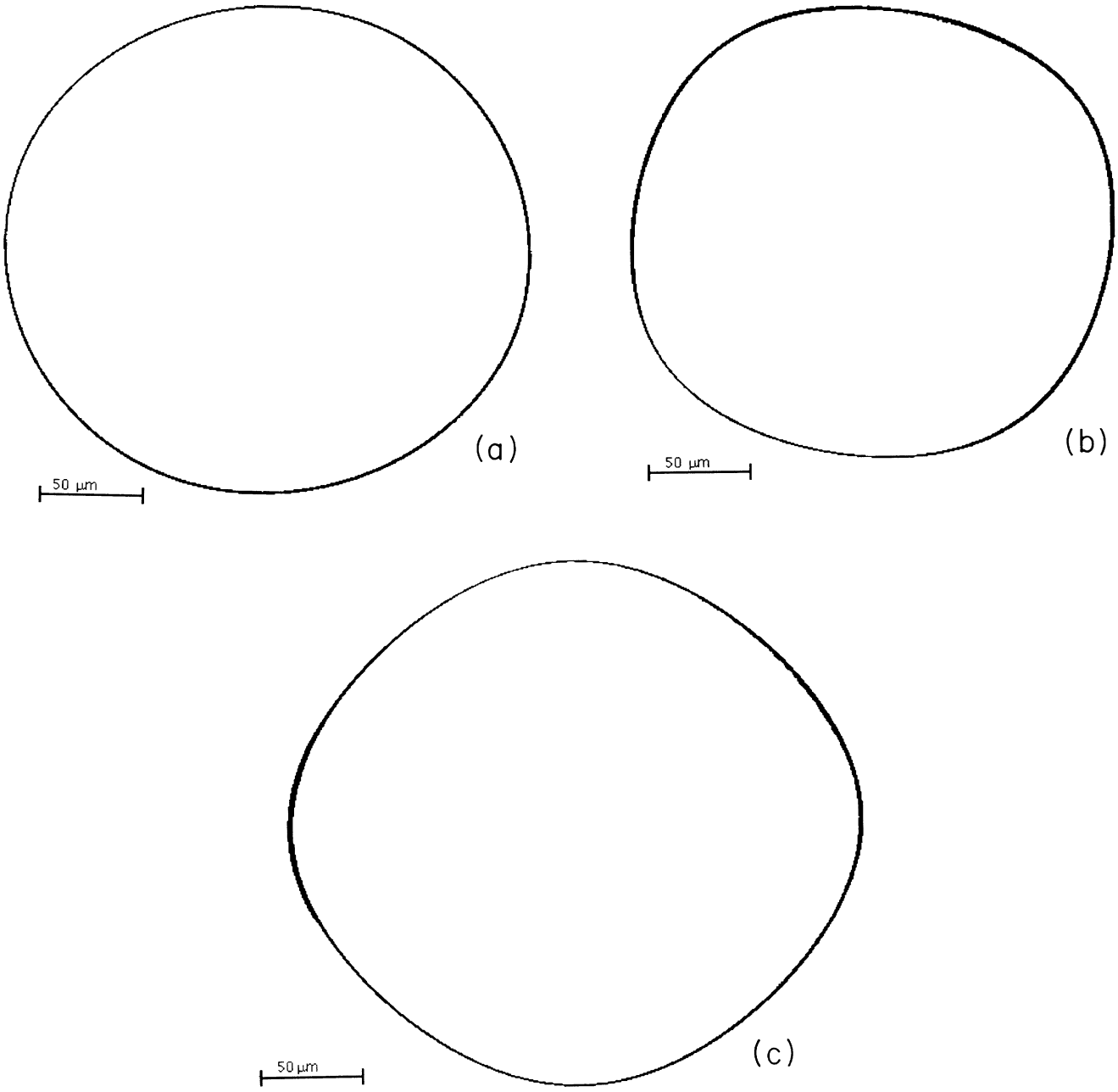

FIG. 8. Binary video images of crystals of (a) SCN, (b) PVA, and (c) PVA-ethanol. After thresholding of the digitized image, as described in the text, we highlighted all pixels above the threshold by changing their intensity values to black. The large asymmetry of PVA is visible in (b) and (c).

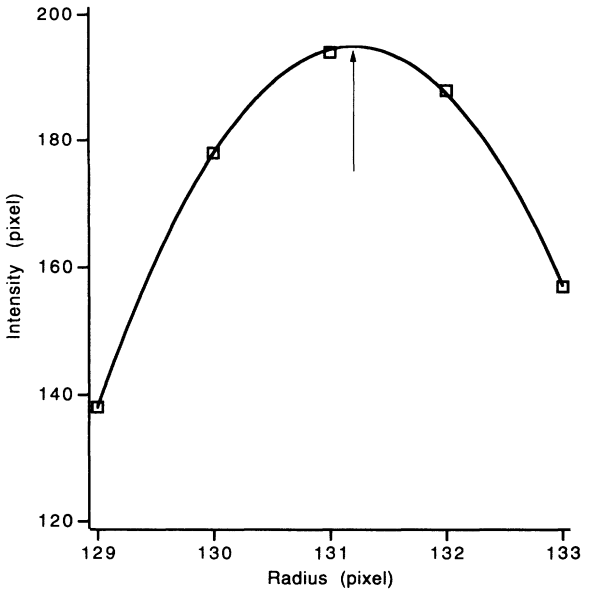

FIG. 9. Radial intensity profile of a SCN crystal interface obtained as described in the text. The dashed line is the fitted parabola, and the arrow shows the interpolated position of the center of the interface.

negligible. The resulting polar coordinates of the interface can be determined with an accuracy of about 0.2 pixels. The parabolic intensity profile analysis procedure seems to reduce the noisiness of the interface coordinates in comparison to Dougherty and Gollub's data [11, 12].

Typical plots of the extracted polar coordinates for the three materials are shown in Fig. 10. Note the clear fourfold shape anisotropy, but also the presence of a weaker twofold Fourier component, similar to observations of Dougherty and Gollub [11, 12]. Because of this twofold component we Fourier analyze our data instead of fitting them directly to the shape of a crystal with purely fourfold surface-tension anisotropy as given in Eqs. (2.4) and (2.5). In the fit, we used the first eight Fourier modes of the cosine transform

$$r_i(\phi_i) = a_0 + \sum_n a_n \cos(n\phi_i + \delta_n), \tag{3.2}$$

where a_n is the amplitude of the nth mode and δ_n is the corresponding phase angle.

D. Experimental results

In Fig. 11 we show the Fourier amplitude ratios a_n/a_0 determined from the analysis of the three interfaces shown in Fig. 8. These ratios are equivalent to the shape anisotropies s_n introduced in Eq. (2.6). The Fourier data show generic features we see in all of our experimental runs. Only the n=2, 3, 4, 6, and 8 modes have measurable amplitudes once the crystal has equilibrated. At the beginning of each experiment the n=2 mode is dominant but it decays to values well below the n=4 amplitude after the initial equilibration. The fourfold component, in contrast, is remarkably stable. The time dependence of the amplitudes of these two modes for the case of PVA–1%-ethanol sample is shown in Fig. 12. The initial equilibration period is about 30 min for pure SCN and PVA and is considerably longer for the binary system. This is because in pure materials relaxation occurs via thermal diffusion while in binary mixtures chemical diffusion dominates the equilibration.

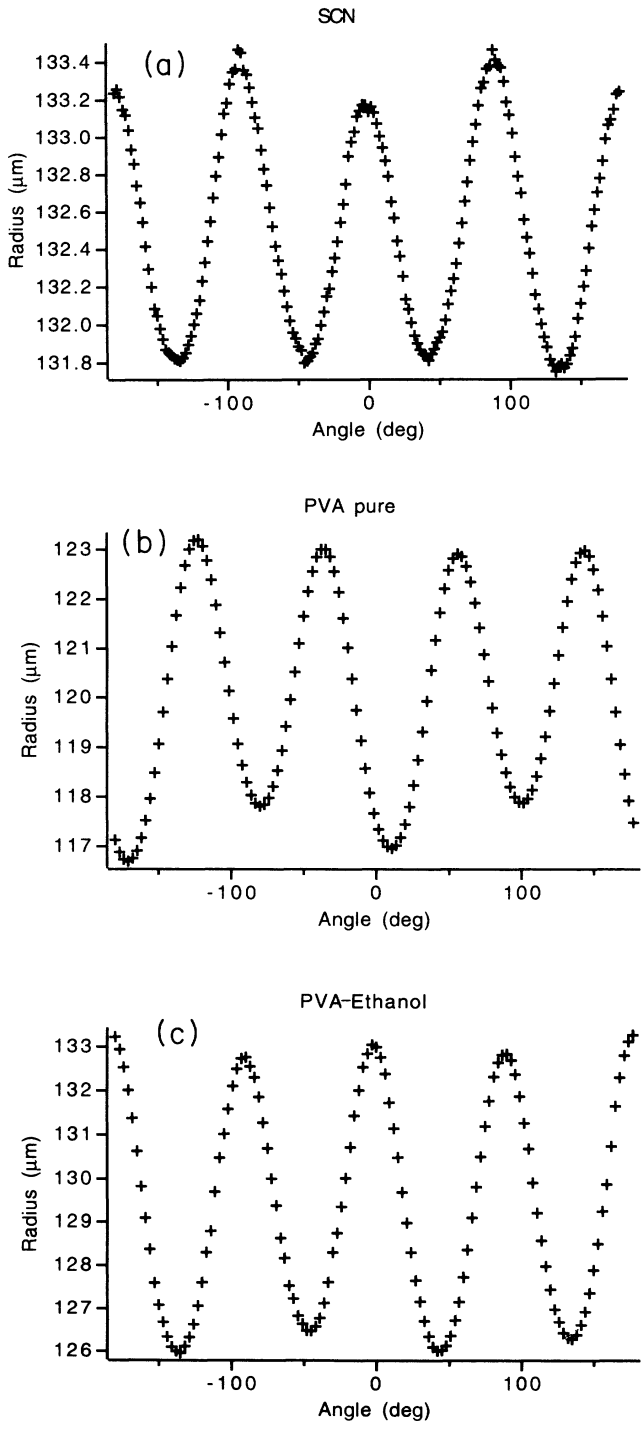

FIG. 10. Polar plot of the extracted interface coordinates of the three crystals shown in Fig. 8.

The presence of the n=2, 3, 4, and 6 modes is consistent with the shape of a three-dimensional crystal with cubic symmetric surface tension when seen from different directions as shown in Fig. 5. Unfortunately, the amplitudes of the n=2, 3, and 6 modes are not steady or large enough to deduce the precise orientation of the seed from them. As mentioned above, we try to check

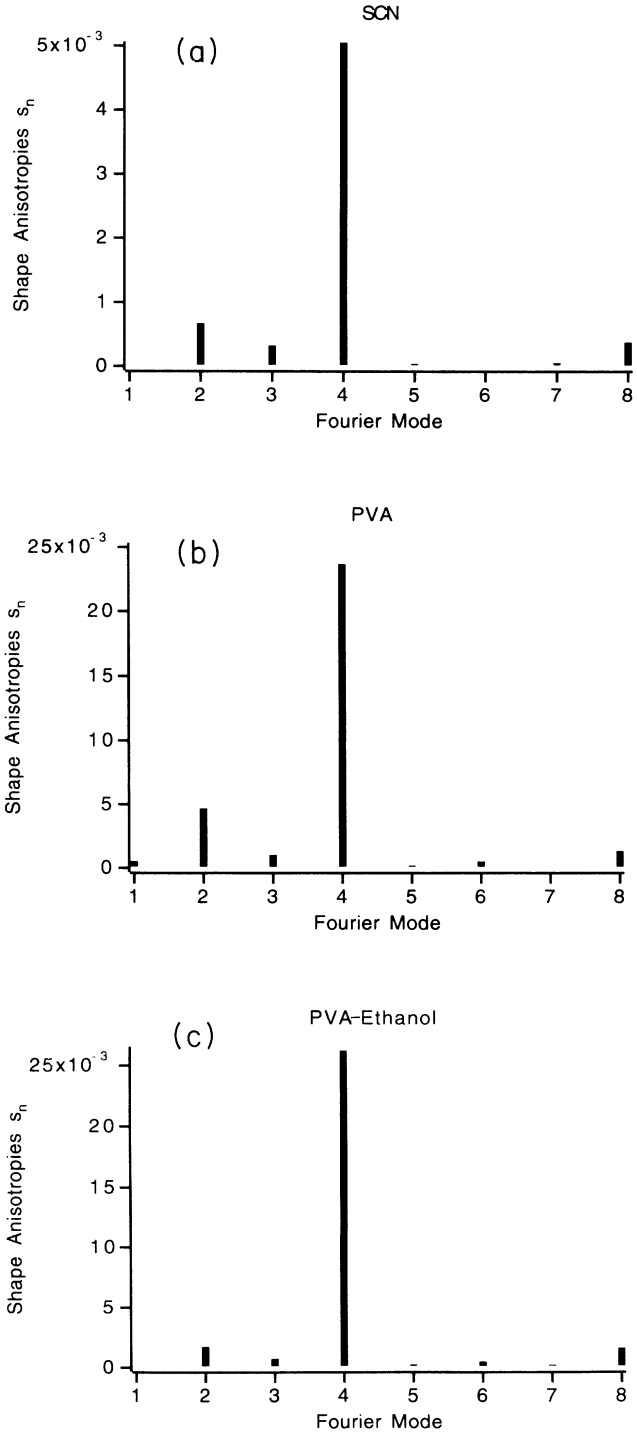

FIG. 11. Fourier amplitude ratios $s_n = a_n/a_0$ of the three interfaces of Fig. 10.

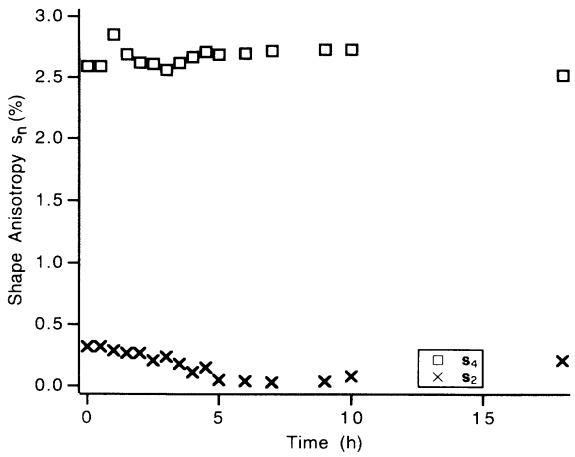

FIG. 12. Time dependence of the $n = 2$ and 4 mode amplitudes during an experimental run with the PVA-ethanol mixture.

the orientation of our seeds by making them go unstable and observing the orientation of the resulting dendritic branches as shown in Fig. 7. For seeds oriented close to the [100] direction, the value of the fourfold component in PVA is considerably larger than for seeds oriented along [111]. The value of s_4 changes with orientation from 2.4% to 1.3%. This ratio is roughly equal to $1/\sqrt{3}$ and also consistent with changes due to orientation. We therefore select the largest values of s_4 even in SCN where we had no means of observing the orientation.

As our calculation in Sec. II showed, the effects of thermal gradients can be neglected if the temperature gradient at the crystal surface is smaller than the critical gradient. For a crystal of $\sim$ 100 μm radius the critical gradient in SCN is 6.1×10^{-3} mK/μm and in PVA is 4.1×10^{-3} mK/μm. These values are an order of magnitude larger than the thermal gradient in our thermostat and we can therefore neglect their effects on our results.

IV. DISCUSSION AND CONCLUSIONS

From the experiments described in the preceding section, we conclude that the surface tension anisotropies ε_4 for SCN, PVA, and PVA–1%-ethanol are (0.55±0.15)%, (2.5±0.2)%, and (2.6±0.2)%, respectively, as shown in part (b) of Table I. Our SCN result agrees with that of Glicksman and Singh [14]. For PVA, however, our result disagrees with both previous measurements; it is approximately two times smaller than that of Glicksman and Singh [14] and four times larger than that of Dougherty [12]. Moreover, we find that the addition of 1% ethanol to the PVA has no significant effect on ε_4.

In order to compare values of σ^*_{theor} deduced from measurements of the surface tension anisotropy (via the theoretical MST relation illustrated in Fig. 1) with σ^*_{expt} values determined from observations of growing dendrites, several factors must be considered.

(1) The relation between σ^*_{theor} and α depends somewhat on the Péclet number $p = \rho v/2D$ as illustrated by

the results of Barbieri and Langer [8] for p=0 and 0.25 in Fig. 1. We have therefore included the range of the Péclet number for each determination of σ^*_{expt} in Table II. Since for all the measurements $p \ll 0.25$, we used the p=0 results to find σ^*_{theor}.

(2) The theoretical results shown in Fig. 1 are for the symmetric model in which $\mu = D_s C_s / D_l C_l = 1$. ($D$ is the thermal or chemical diffusion constant, C is the specific heat, and s and l refer to solid or liquid, respectively.) The equivalent asymmetry parameter for binary mixtures is $\mu = D_s/D_l$. Barbieri and Langer [8] have shown that for any value of μ

$$\sigma^*(\mu) = [2/(1+\mu)]\sigma^*(\mu = 1). \tag{4.1}$$

Since experimental values of D_s are generally not available, we have followed the conventional procedure of letting $\mu = 1$ for pure materials (symmetric model) where growth is controlled by thermal diffusion, and $\mu = 0$ for binary mixtures or solutions (one-sided model) where chemical diffusion dominates, so that $\sigma^* = 2\sigma^*(\mu = 1)$. The values of σ^*_{theor} shown in Table I therefore correspond to the 3D, $p = 0$ axisymmetric numerical results in Fig. 1 for pure materials, and to twice those values for binary mixtures and solutions.

Table I clearly illustrates that the values of σ^*_{theor} deduced from anisotropy measurements and σ^*_{expt} determined from observations of dendritic growth differ significantly for both SCN and PVA, by a factor of approximately 2, and in opposite directions. Figure 13 represents the information of Table I graphically. The noticeable discrepancies are well beyond the reported experimental errors, although the reported values of σ^*_{expt} for SCN and PVA include no error estimates. We note that only for the solution growth cases of NH_4Br and HET do σ^*_{expt} and σ^*_{theor} appear to agree, and for NH_4Br Maurer, Perrin, and Tabeling [23] found values of $\rho^2 v$ significantly smaller than those reported in Ref. [11]. (The ice result cannot be considered significant in view of the preliminary nature of the measurement of ε_6 [24].)

We are therefore led to the essential question of whether or not these discrepancies can be reconciled with the basic approach of MST. Assuming that the discrepancies are real and are not produced by experimental artifacts such as convection, there remain several possible ways in which the MST predictions might be modified.

First, the three-dimensional predictions shown in Fig. 1 assume axisymmetric dendrites [8] while real 3D dendrites exhibit pronounced anisotropy around their axes. The consequences of this axial anisotropy for MST have not yet been fully analyzed. Preliminary results indicate, however, that deviations of σ^*_{theor} from the axisymmetric values given here are small [25].

Second, since the dendritic-growth experiments summarized in Table II were all performed (necessarily) with nonzero growth velocities, the values of σ^*_{expt} they produce must include kinetic effects which should be included in the comparison.

Third, we note that the analysis underlying the MST predictions of Fig. 1 assumes a single nearly parabolic needle crystal without sidebranches, boundaries, or other neighboring dendrites. Brener and his co-workers have shown that a single dendrite growing in a channel [5] or a dendrite surrounded by other dendrites [26] may undergo morphological transitions to other growth forms, and Oswald, Malthête, and Pelce [27] have reported observing morphological transitions in HET which they attribute to such confinement effects.

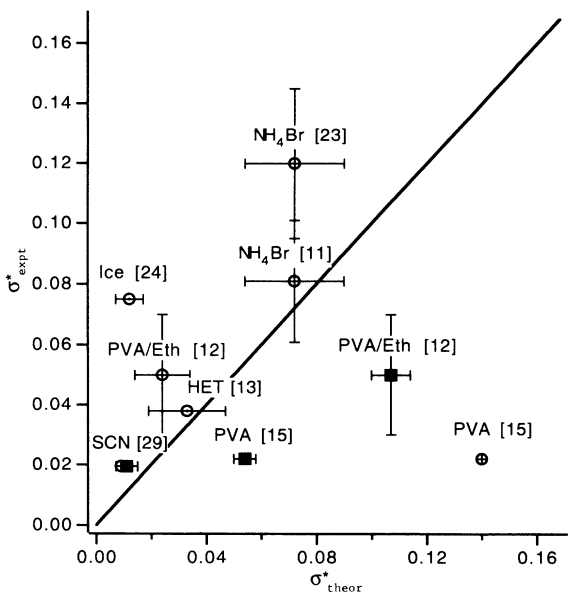

FIG. 13. Plot of σ^*_{expt} vs. σ^*_{theor}. Values of σ^*_{expt} are based on experimental measurements of v and ρ, while the results of σ^*_{theor} are derived from measured surface-tension anisotropies. Circles are data points from previous anisotropy measurements, while the black squares are based on our data. Whenever available, error bars for both σ^*_{expt} and σ^*_{theor} are included. Errors in σ^*_{expt} are due to uncertainty in v, ρ, and material parameters, errors in σ^*_{theor} are based on uncertainty in surface-tension anisotropy. References on the data points refer to the source of σ^*_{expt}. The straight line, indicating perfect agreement with MST, is given as a guide to the eye.

Fourth, Brener has noted that MST predictions based on the usual approximation of Eq. (2.2) may be significantly modified by the presence of higher harmonics. From our determinations of s_4 and s_8 for SCN and PVA illustrated in Fig. 8, we have estimated ε_8 and $\alpha_8 = 63\varepsilon_8$ as $\alpha_8 = +0.016 \pm 0.02$ for SCN, and $\alpha_8 = -0.057 \pm 0.02$ for PVA. By including both α_4 and α_8 in a 2D numerical MST computation (program of Ben Amar), Brener found that σ^*_{theor} for SCN is increased by $\sim 50\%$, with a much smaller correction for PVA [28].

The discrepancies between σ^*_{expt} and σ^*_{theor} shown in Table I and Fig. 13 may be due, at least in part, to these considerations. However, in view of the results for SCN and PVA described in this report, the correctness of MST in its present form cannot realistically be viewed as being confirmed by experiment.

ACKNOWLEDGMENTS

We thank X.W. Qian for his participation in the early phases of this experiment, H. Levine for providing the

computer program used to generate the 2D numerical σ^*_{theor} data in Table I, M. Ben Amar for providing the 3D axisymmetric σ^*_{theor} data, and E.A. Brener for analyzing the contributions of ε_8 anisotropy. We also thank O. Martin, J. Koplik, A. Dougherty, J. Gollub, M. Glicksman, Y. Couder, and P. Tabeling for helpful discussions. This research was supported by the U.S. Department of Energy under Grant No. DE-RG02-84-ER45132.

[1] G.P. Ivantsov, Dokl. Akad. Nauk SSSR **58**, 567 (1947).
[2] J.S. Langer, Rev. Mod. Phys. **52**, 1 (1980).
[3] M.E. Glicksman, R.J. Schaefers, and J.D.Ayers, Metall. Trans. A **7**, 1747 (1976).
[4] D.A. Kessler, J. Koplik, and H. Levine, Adv. Phys. **37**, 255 (1988).
[5] E.A. Brener and V.I. Melnikov, Adv. Phys. **40**, 53 (1991).
[6] J.S. Langer, Science **243**, 1150 (1989).
[7] P. Pelce, *Dymanics of Curved Fronts* (Academic, New York, 1988).
[8] A. Barbieri and J.S. Langer, Phys. Rev. A **39**, 5314 (1989); A. Barbieri, D.C. Hong, and J.S. Langer, *ibid.* **35**, 1802 (1987).
[9] D.A. Kessler and H. Levine, Phys. Rev. B **33**, 7867 (1986).
[10] M. Ben Amar (private communication).
[11] A. Dougherty and J.P. Gollub, Phys. Rev. A **38**, 3043 (1988).
[12] A. Dougherty, J. Cryst. Growth **110**, 501 (1991).
[13] P. Oswald, J. Phys. (Paris) **49**, 1083 (1988).
[14] M.E. Glicksman and N.B. Singh, in *Rapidly Solidified Powder Aluminum Alloys*, edited by M.E. Fine and E.A. Starke, Jr. (ASTM, Philadelphia, 1986), p. 44.
[15] M.E. Glicksman and N.B. Singh, J. Cryst. Growth **98**, 277 (1989).
[16] W.W. Mullins, in *Metal Surfaces: Structure, Energetics and Kinetics* (American Society of Metals, Metals Park, OH, 1963), p. 44.
[17] Note that the dimensionless undercooling is frequently defined as $\Delta' = (T_m - T)/(L/C_p)$, which gives $R^* = d_0/\Delta'$ in two dimensions or $R^* = 2d_0/\Delta'$ in three dimensions (Ref. [2]).
[18] P.W. Voorhees, S.R. Coriell, G.B. McFadden, and R.F. Sekerka, J. Cryst. Growth **67**, 425 (1984).
[19] W.H. Press, B.P. Flannery, S.A. Teukolsky, and W.T. Vetterling, *Numerical Recipes* (Cambridge University Press, Cambridge, England, 1986), p. 588ff.
[20] M. Muschol, Ph.D. thesis, City University of New York, 1992.
[21] J.W. Cahn and D.W. Hoffman, Acta Metall. **22**, 1205 (1974).
[22] W. Kurz and J.S. Fisher, *Fundamentals of Solidification*, (Trans. Tech., Rockport, MA, 1986), p. 57.
[23] J. Maurer, B. Perrin, and P. Tabeling, Europhys. Lett. **14**, 575 (1991).
[24] K. Koo, R. Ananth, and W.N. Gill, Phys. Rev. A **44**, 3782 (1991).
[25] D.A. Kessler and H. Levine, Phys. Rev. A **36**, 4123 (1987).
[26] E.A. Brener, H. Müller-Krumbhaar, and D. Temkin, Europhys. Lett. **17**, 535 (1992).
[27] P. Oswald, J. Malthête, and P. Pelce, J. Phys. (Paris) **50**, 2121 (1989).
[28] E.A. Brener (private communication).
[29] M.E. Glicksman and S.C. Huang, Acta Metall. **29**, 701 (1981).
[30] H. Honjo and Y. Sawada, J. Cryst. Growth **58**, 297 (1982).
[31] T. Fujioka, Ph.D. thesis, Carnegie-Mellon University, 1978.
[32] J.P. Franck and J. Jung, J. Low Temp. Phys. **64**, 165 (1986).
[33] J.H. Bilgram, M. Firmann, and E. Hurlimann, J. Cryst. Growth **96**, 175 (1989).
[34] R.J. Schaefer, M.E. Glicksman, and J.D. Ayers, Philos. Mag. **32**, 725 (1975).
[35] C.A. Wulff and E.F. Westrum, Jr., J. Phys. Chem. **67**, 2376 (1963).
[36] N.B. Singh and M.E. Glicksman, J. Cryst. Growth **98**, 573 (1989).

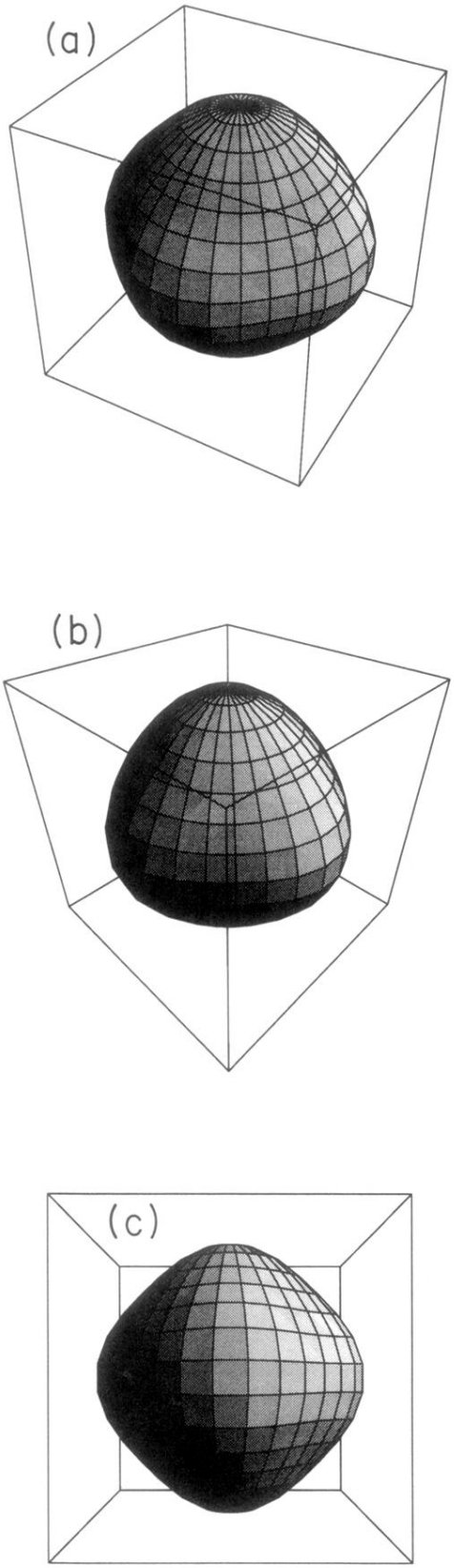

FIG. 5. Three views of the three-dimensional anisotropic surface tension function $\gamma(\theta, \phi)$ of Eq. (2.16) for $\varepsilon_4 = 0.05$. In (b), the normal is along a [111] axis, while in (c) it is along a [100] axis.

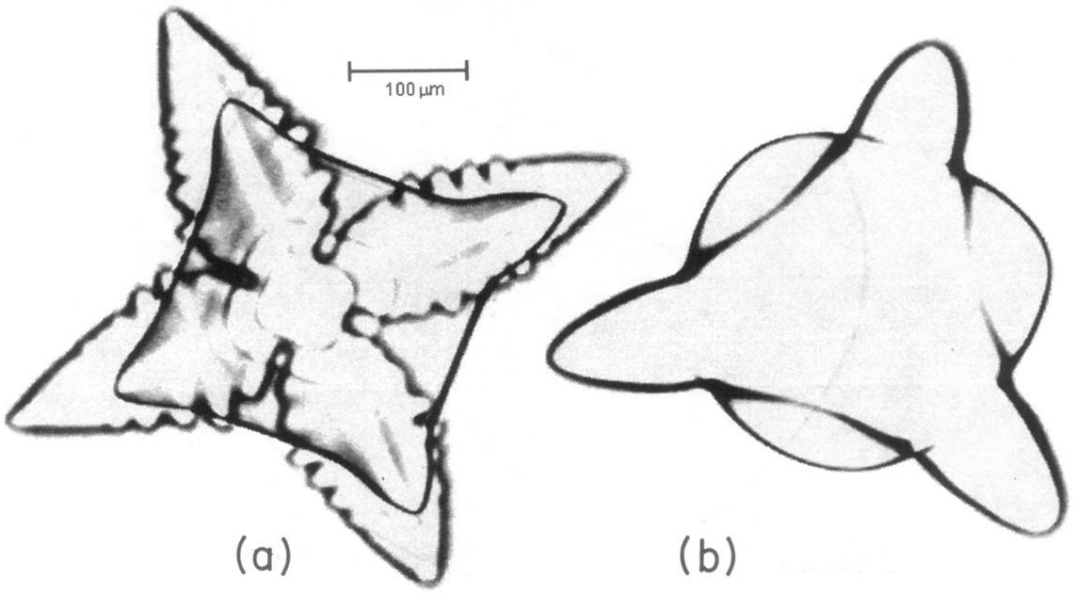

FIG. 7. Images of PVA crystals following a sudden temperature decrease. The fourfold symmetry of (a) indicates that this crystal is oriented with a [100] axis normal to the image, while the threefold symmetry of (b) indicates that a [111] axis is normal to the image.